Bulletin of the Seismological Society of America, Vol. 96, No. 4A, pp. 1383–1395, August 2006, doi: 10.1785/0120050162

Region-Specific Key Seismic Parameters for Earthquakes in Northern Iran

by Dariush Motazedian

Abstract Strong-motion accelerograms recorded within northern Iran are used to examine the propagation characteristics of shear wave, including geometric spreading behavior, Q-value, κ_0, and horizontal-to-vertical (H/V) ratio. These region-specific key seismic parameters are estimated from 259 three-component records of 22 earthquakes with magnitude ranging from **M** 4.9 to **M** 7.4 in northern Iran. The geometric spreading follows a trilinear behavior with a strong postcritical reflection from the Moho. The first and second hinges of the trilinear behavior are at 75 and 150 km, respectively. The associated Q-value, based on the vertical component is $Q = 87 f^{1.46}$. κ_0 value for vertical and horizontal components are 0.03 and 0.05, respectively. Because of lack of station-specific site information, the H/V ratio is considered to be a rough estimation of generic site amplification. The obtained region-specific parameters are used to estimate the average stress drop based on three stochastic modeling approaches. Stochastic point-source modeling suggests a Brune stress drop of 125 bars, whereas stochastic finite-fault modeling based on static and dynamic corner frequency approaches suggests a stress drop of 68 bars.

Introduction

Iran has experienced a high level of seismicity, including several catastrophic earthquakes with thousands of casualties (e.g., Bam, 2003, **M** 6.5; Manjil, 1990, **M** 7.4; Tabas, 1978, **M** 7.4; etc.). The seismic source and wave propagation characteristics in Iran are complex because of hazard contributions from distinct seismotectonic regions, all of which behave differently in terms of their seismic source and ground-motion propagation characteristics (e.g., Stoklin, 1968; Takin, 1972; Berberian, 1976; Nowroozi, 1976; Khademi and Nayeri, 1997; and Mirzaei *et al.*, 1999). The focus of this article is on 22 earthquakes in northern Iran, listed in Table 1 and shown in Figure 1. These earthquakes are located in similar seismotectonic settings.

To enable reliable seismic-hazard estimation for the region, the study of region-specific seismic-source and wave-propagation parameters, in addition to seismic-site effects, is a priority for research. Region-specific parameters can further be used to predict average expected ground-motion amplitudes. The approach taken in this study is to use the results of empirical analyses of strong-motion records to formulate the basic seismic characteristics. Empirical data are used to examine the seismic-propagation characteristics of ground motions, such as geometric spreading behavior, anelastic attenuation (Q-value), κ_0, and site-amplification factor, each described separately in the following sections. Then, these key region-specific parameters are used to estimate stress drop, based on stochastic point-source and finite-fault modeling approaches. In the application of finite-fault modeling both static and dynamic corner frequency approaches (Motazedian and Atkinson, 2005b) are applied.

Database

The Building and Housing Research Centre of Iran (BHRC) operates more than 1000 strong-motion stations composed of three-component accelerographs. The network has recorded more than 2000 earthquakes since its inception in 1973 (BHRC, 2005). The BHRC ground-motion database has been growing steadily during the past decade because of increasing numbers of strong-motion stations and the occurrence of large-magnitude earthquakes. One particular example, the **M** 6.3 Kojour earthquake in northern Iran, was recorded on approximately 139 three-component BHRC strong-motion stations.

In this study, Fourier and response spectra of 761 acceleration time series recorded by 259 three-component BHRC instruments for the 22 earthquakes presented in Figure 1 and Table 1 were computed and analyzed. In the course of data processing, the shear-wave portion of signal (including direct, reflected, and refracted phases) were windowed for all time series of events at distances up to 200 km. For each record the general procedures are: (1) tapering the windowed time series using a 5% cosine taper on each end of the signal; (2) zero-padding the time series to the next greatest power of 2; (3) transforming to frequency domain by fast Fourier transform; (4) removing instrument response; (5) transferring to time domain by applying the inverse Fourier transform; (6) calculating response spectra for 5% damping from corrected acceleration time series; (7) discarding the frequencies with a signal to noise ratio less than 2 in the frequency domain, where the pre-event noise is available

Table 1
Study Earthquakes Recorded by BHRC Accelerographic Stations in Northern Iran

Event No.	yyyy-mm-dd	hh:mm:ss	Latitude	Longitude	**M***	Depth (km)	Reference†
1	1980-07-22	5:17:06	37.36	50.35	5.5	37	ISC,HRVD
2	1980-12-03	4:26:15	37.17	50.47	5.3	44	ISC,NEIS,HRVD
3	1985-10-29	13:13:40	36.75	54.81	6.1	15	NEIS,HRVD
4	1987-04-10	6:43:20	37.21	57.70	5.1	6	ISC,HRVD
5	1990-01-20	1:27:10	35.89	53.00	5.9	25	ISC,HRVD
6 (Manjil)	1990-06-20	21:00:11	36.99	49.35	7.4	15	ISC,HRVD
7	1990-06-24	9:46:01	36.88	49.42	5.3	10	ISC,HRVD
8	1990-07-06	19:34:54	36.91	49.30	5.3	35	ISC,NEIC
9	1991-11-28	17:19:53	36.92	49.60	6.5	16	ISC,NEIC
10	1995-10-15	6:56:34	37.05	49.47	5.2	33	HRVD
11	1996-01-03	8:42:26	38.99	48.72	5.3	56	NEIS,HRVD
12	1997-02-04	9:53:55	37.56	57.30	5.4	10	NEIS,HRVD
13 (Garmkhan)	1997-02-04	10:37:47	37.66	57.29	6.5	11	NEIS,HRVD
14	1997-02-05	7:53:45	37.63	57.59	5.2	10	NEIS,HRVD
15	1997-02-28	12:57:45	38.08	48.05	6.1	10	NEIS,HRVD
16	1997-03-02	18:29:42	38.00	47.89	5.3	10	ISC,NEIS,HRVD
17	1998-07-09	14:19:18	38.72	48.51	5.9	26	NEIS,HRVD
18	1998-08-04	11:41:59	37.34	57.27	5.3	33	NEIS,HRVD
19	1999-11-19	4:40:24	37.34	54.40	5.4	35	NEIS,HRVD
20	1999-11-26	4:27:24	36.92	54.90	5.3	33	NEIS,HRVD
21	2000-08-16	12:53:02	36.72	54.36	4.9	33	NEIS,HRVD
22 (Kojour)	2004-05-28	12:38:46	36.52	51.82	6.3	17	ISC,NEIS,HRVD

*M is moment magnitude based on the Harvard Centroid Moment Tensor database.
†ISC, International Seismological Centre; HRVD, Harvard Seismology; NEIS, National Earthquake Information Centre.

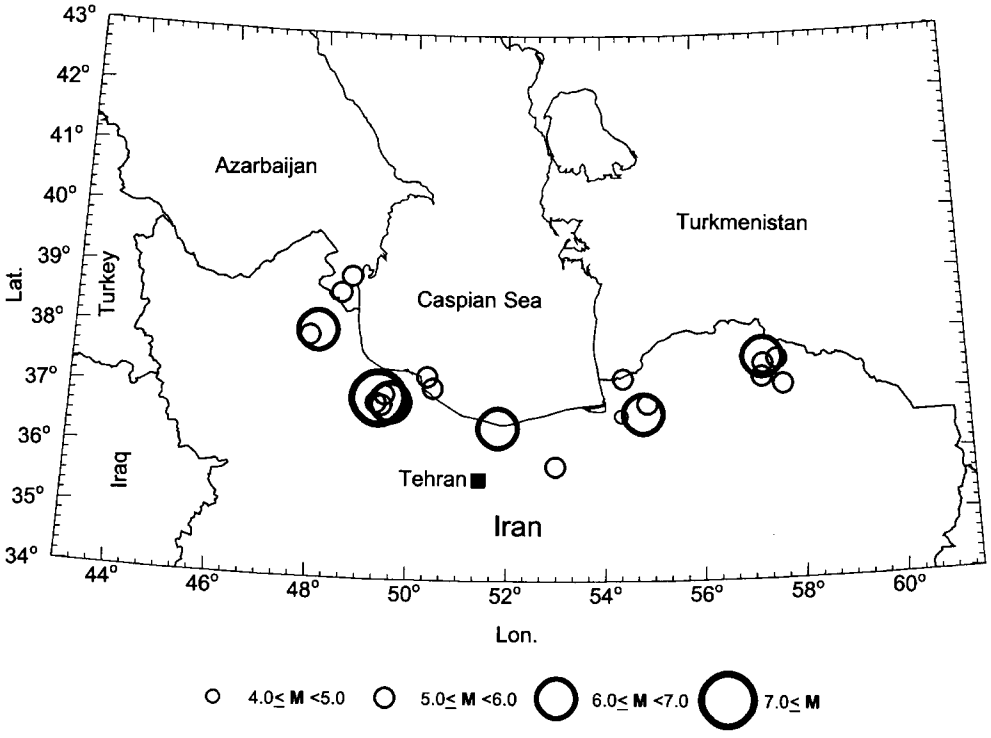

Figure 1. Distribution of the study earthquakes in northern Iran recorded by the Building and Housing Research Centre (BHRC) strong-motion stations.

(the record is discarded where the pre-event noise is not available and the quality of signal is poor); and (8) smoothing the Fourier spectra. The spectra were smoothed by using a weighted nine-point smoothing algorithm, and tabulated over frequencies from 0.1 Hz to 20 Hz, where available. Both vertical and horizontal components were compiled. The main use of the Fourier amplitude spectral database is in the investigation of attenuation characteristics of the events as discussed in the following sections.

Iranian earthquake magnitudes are generally compiled based on teleseismic earthquake records located by international agencies; thus, large differences exist between earthquake magnitude scales, in particular, for smaller events. To avoid the inclusion of the resulting uncertainty in magnitude, the only magnitude used in this study is the moment magnitudes based on the Harvard Centroid Moment Tensor database (HRVD-CMT), which provides a uniform characterization of amplitude level for all events on a common scale. The magnitude-distance distribution of data in northern Iran compiled for this study is shown in Figure 2. The empirical database is poor at higher magnitudes and dominated by small to moderate events ($M < 6.5$). This places significant constraints on the use of the empirical database in ground-motion studies.

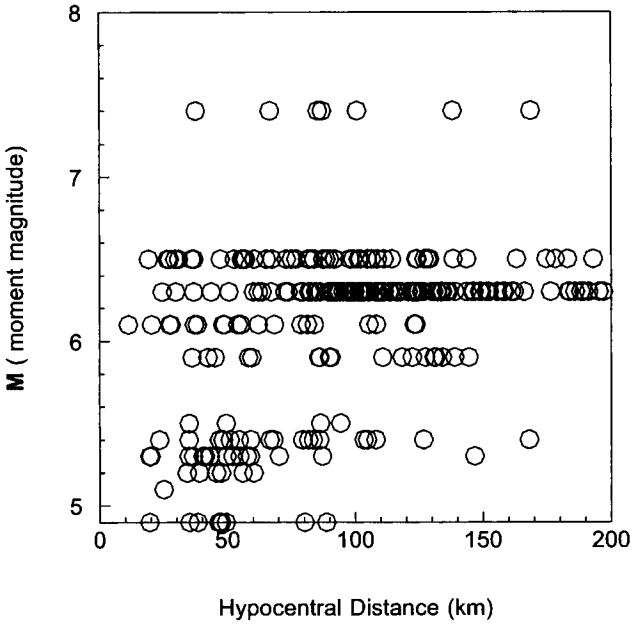

Figure 2. Magnitude-distance distribution of study accelerograms recorded by the BHRC in northern Iran.

Q-Value

Q-value, which is inversely related to the anelastic attenuation of seismic waves, varies from place to place, depending on the seismotectonic features (e.g., Aki, 1980). Knowledge of anelastic attenuation is important because anelastic attenuation determines the shape of the high-frequency spectrum whereas the absolute level of the spectrum is controlled by the stress drop. Anelastic attenuation has been widely investigated in various regions of the world by using direct regression on the shear-wave Fourier amplitude spectra (e.g., Raoof *et al.*, 1999; Sokolov *et al.*, 2002; Atkinson, 2004; Motazedian and Atkinson, 2005a). In this study, regression analysis of the Fourier amplitude spectra is used to determine anelastic attenuation based on the previously mentioned database. Regression is performed by the maximum likelihood method by using the algorithm of Joyner and Boore (1993, 1994). In general, the following form is considered for the observed Fourier amplitudes at each frequency.

$$\log A_{ij} = c_1 + c_2(M_i - 4) + c_3(\mathbf{M} - 4)^2 + b \log R_{ij} + c_4 R_{ij} + \log S, \quad (1)$$

where A_{ij} is the observed spectral amplitude of earthquake i at station j. R_{ij}, b, **M** and S are the hypocentral distance, the geometric spreading coefficient, the moment magnitude and the site effects, respectively. c_1 through c_4 are empirically determined coefficients. In this step the main focus is on the anelastic coefficient c_4, which is inversely related to the quality factor, Q:

$$Q = (\pi f)/(\ln (10) c_4 \beta), \quad (2)$$

where β is the shear-wave velocity and f is frequency in hertz (e.g. Atkinson and Mereu, 1992). Note that there is a possible trade-off between the source and geometric spreading terms in the regression procedures (Joyner and Boore, 1993, 1994). Two approaches were considered to avoid distance-magnitude trade-offs. (1) Equation (1) was applied to a single earthquake with a very rich database (the **M** 6.3 Kojour earthquake). Thus, the first three terms are constant and there is no trade-off between the source term and the other regression terms. The Kojour earthquake is considered for this approach because it was recoded on 139 three-component BHRC strong-motion stations, which covers more than 50% of the study database (417 of 792 vertical and horizontal records). Thus, this earthquake by itself provides a reasonable database for regression analyses. (2) The source terms were replaced by dummy variables in the regression procedures.

Figure 3, which plots vertical peak ground acceleration (PGA) versus distance for a subset of data (earthquakes with magnitude from **M** 6.3 to **M** 6.5), clearly shows the different behavior of b-values at different distances and suggests a possible trilinear behavior for geometric spreading. Thus, the geometric spreading coefficient (b-value) should be determined at different distances for any possible multisegment behavior due to postcritical reflection effect from Moho (Burger *et al.*, 1987) and domination of multiply reflected and refracted shear waves at larger distances (Hermann and Kijko, 1983). Because of the lack of information on BHRC site conditions, and because the vertical component is af-

fected less by site conditions than horizontal components, using vertical components in this step minimizes the effect of the site on the results. Thus, in this step, equation (1) is only applied to vertical components.

A general trilinear behavior for geometric spreading is considered for the regression analysis on 139 vertical component records of the Kojour earthquake. R_1, the first hinge point, is the distance between the source and where the postcritical effect from Moho appears. R_2, the second hinge point, is the distance where multiply reflected and refracted shear waves dominate the signal. b_1, b_2, and b_3 are the b-values for distances from the source to R_1, R_1 to R_2, and beyond R_2. A wide range of values were considered for these parameters. R_1, R_2, b_1, b_2, and b_3 varied from 40 to 90 km, 60 to 160 km, -1.3 to -0.5, -0.5 to 0.5, and -0.5 to 0.5, respectively. The maximum likelihood method was applied to all possible combination of R_1, R_2, b_1, b_2, and b_3 (about 20,000 combinations). For each combination the regression results were compared with the observed records by calculation of residuals, where the residual is defined as the log of observed Fourier amplitudes minus the log of Fourier amplitudes predicted by equation (1). The best distribution of residuals is for the case where $R_1 = 70$ km, $R_2 = 150$ km, $b_1 = -0.6$, $b_2 = +0.2$, and $b_3 = -0.1$. The positive b-value for the second segment suggests that a strong postcritical reflection effect from Moho appears at 70 km. A similar positive behavior for b-value was also discovered by Atkinson (2004) for eastern North America. The results of both approaches, using dummy variables for the source terms and regression on a subset of data, which includes only the Kojour earthquake, are similar. The symmetric behavior of residuals versus distance without any specific trend, as shown in Figure 4, confirms that the selected b-values are reasonable for the study region.

Having a fixed b-value for different segments of the trilinear model of geometric spreading, the Q-value can be determined by using equation (2). To avoid any potential magnitude-distance trade-offs in this step the source terms were replaced with dummy variables in the regression procedures. The obtained Q-value for northern Iran is shown in Figure 5. The behavior of Q-values is represented by a U-shaped curve, following

$$\log(Q) = 1.99(\log f)^2 - 0.67(\log f) + 2.32. \quad (3)$$

The U-shaped behavior of Q-value has been observed by many investigations such as Aki (1980), Cormier (1982), Boore (2003), and Atkinson (2004). Although the behavior of the Q-value is represented by a U-shaped curve, the Q-values for frequencies above 1.0 Hz, the portion of most interest in frequency space, can be approximated by a straight line as shown in Figure 5. The straight line presented in Figure 5 is given by

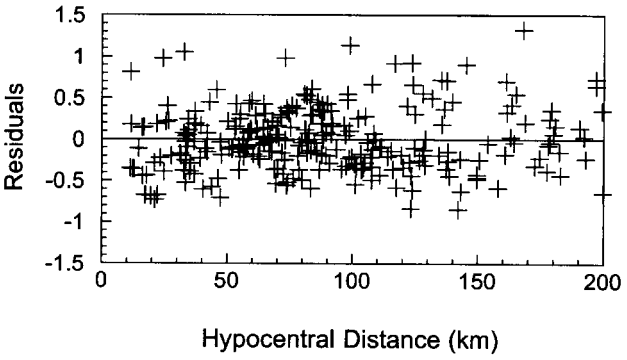

Figure 4. Distribution of residuals versus distance where $R_1 = 70$ km, $R_2 = 150$ km, $b_1 = -0.6$, $b_2 = +0.2$ and $b_3 = -0.1$. Residual is defined as the log of observed Fourier amplitudes minus the log of predicted Fourier amplitudes by equation (1).

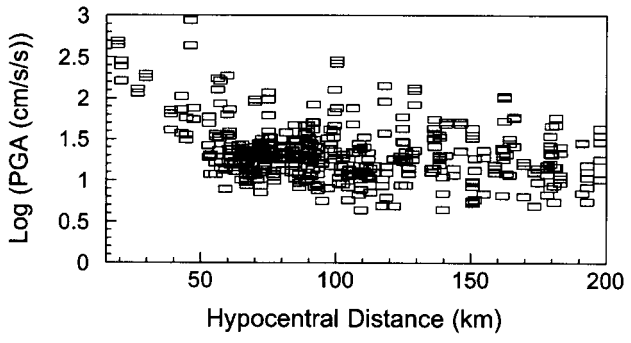

Figure 3. Vertical PGA versus distance for earthquakes with magnitude from **M** 6.3 to **M** 6.5. The different behavior of b-values at different distances is clear.

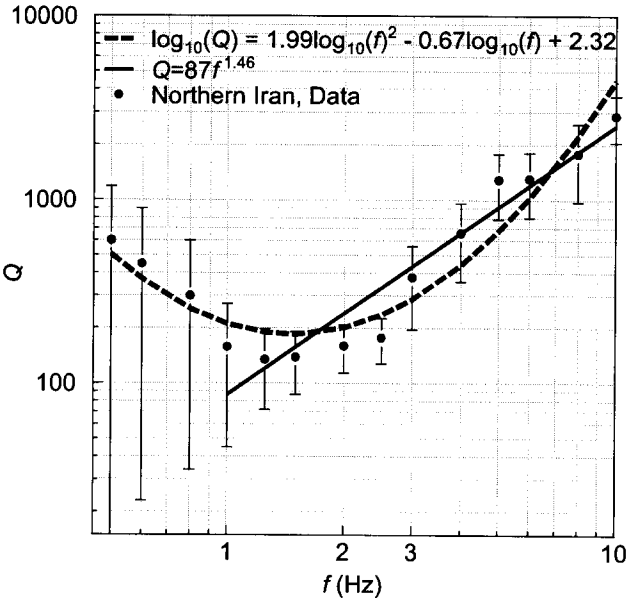

Figure 5. The regional Q-value for northern Iran follows a U-shaped curve. Q-values for frequencies greater than 1.0 Hz can be roughly represented by a straight line given by $Q = 87 f^{1.46}$.

$$Q = 87f^{1.46}. \quad (4)$$

Thus, the behavior of anelastic attenuation versus distance is modeled through Q-values. In the next section the focus is on κ_0, which is considered to represent the near-surface attenuation of seismic wave.

Kappa Factor

High-frequency amplitudes are reduced through the kappa operator (Anderson and Hough, 1984) by applying the factor $\exp(-\pi f\kappa)$. Kappa acts to rapidly diminish spectral amplitudes above some threshold frequency and is believed to be primarily a site effect (Atkinson, 2004). In this study, the kappa factor for each individual record is obtained from the slope of the smoothed log acceleration Fourier spectral amplitude at high frequencies, generally greater than 5 Hz, where frequency is in linear scale. A least-squares fit to the spectrum of each record is determined. Kappa factors calculated for the vertical component of all records versus distance are shown in Figure 6. As expected, κ_{ij} is a distance-dependent parameter because of the frequency dependence of anelastic attenuation. The best-fit line to the distribution of kappa versus distance is fit to the form $\kappa = \kappa_r R + \kappa_0$. The best-fit coefficients for the vertical component are $\kappa_r = 0.0002$ and $\kappa_0 = 0.029$.

The kappa factor for the horizontal components is estimated based on the same procedures. The general trend of kappa versus distance for horizontal components, which is not shown for the sake of brevity, is similar to those of vertical components but with different κ_0 values. The κ_0 for horizontal components is 0.05, which is larger than that of the vertical components. This confirms that the attenuation of higher frequencies is much less on the vertical than the horizontal component, as the vertical component is less sensitive to the variation of shear-wave velocity of near-surface deposits. The clear difference between vertical and horizontal values suggests that κ_0 contains a dependence on near-surface site-specific attenuation effects. The kappa value for northern Iran is intermediate compared with $\kappa_0 = 0.10$ for Turkey (Anderson *et al.*, 2001), which is located immediately to the west of the study region, and $\kappa_0 = 0.02$ to 0.04 for soft rock sites in California (Anderson and Hough, 1984; Boore *et al.*, 1992; Atkinson and Silva, 1997; Boore and Joyner, 1997).

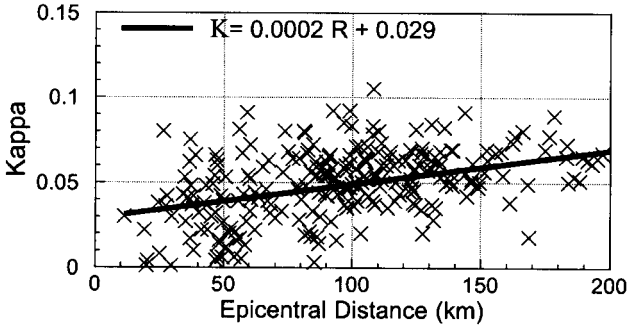

Figure 6. The distribution of kappa factor versus distance for vertical components. The κ_0 for vertical components is 0.03.

Horizontal-to-Vertical (H/V) Ratio

Currently, no specific information regarding the site amplification of BHRC stations exists, but BHRC is currently conducting site-amplification measurements for its strong-motion network. This study does not provide an accurate estimation of site effect for BHRC stations, instead, it provides a rough but useful approximation for the scaling of stress drop in northern Iran. An improvement on this issue will be possible as further studies being conducted by the BHRC establish the seismic-site classification across Iran. The results of this study can easily be adjusted on the availability of the site information when they become available.

Earthquake waves propagate from the source region, where the shear-wave velocity is typically about 3.6 km/sec toward the surface, where the average shear-wave velocity may be as low as 620 m/sec for generic soft-rock sites (Boore and Joyner, 1997). The spectrum is amplified through this velocity gradient by seismic-impedance effects. Amplification effects are observed strongly on the horizontal components, but weakly on the vertical one. Although there is no strong theory behind the H/V ratio method, the ratio of the H/V component of ground motion is generally considered to be a good, if crude, estimate of site amplification, as discussed by Nakamura (1989), Lermo and Chavez-Garcia (1993), Beresnev and Atkinson (1997), Atkinson and Cassidy (2000), and Siddiqqi and Atkinson (2002).

In general, the overall site effect, $S(f)$, is the site amplification, $D(f)$, multiplied by the near-surface attenuation, $\exp(-\pi f\kappa)$ as: $S(f) = D(f)e^{-\pi\kappa f}$. It is common to replace the site amplification, $D(f)$, by the H/V ratio. The most ambiguous part is the κ value that should be used along with the H/V ratio, because both horizontal and vertical components have already gone through surface attenuations, but with different κ values. Although it is assumed that the vertical amplification is negligible compared with the horizontal, yet a considerable near-surface attenuation for vertical component is observed ($\kappa_v = 0.03$ in this study). Because there is no strong theory behind this approach, the decision should be made empirically based on the behavior of overall spectrum at high frequencies, usually more than 5 Hz (G. Atkinson, personal comm.). However, let us consider two extreme cases for vertical κ. (1) In the case of identical κ for both vertical and horizontal components ($\kappa_v = \kappa_h$) the effect of κ values are canceled in the H/V ratio and the $e^{-\pi\kappa_h f}$ is needed to include the near-surface attenuation in the site effect for the horizontal component. This means the site term for the horizontal component is $S(f) = \text{H/V}e^{-\pi\kappa_h f}$ (2) Another extreme case is $\kappa_v = 0 \neq \kappa_h$, then, the near-surface attenuation effect is already included in the

H/V ratio and there is no need for additional $e^{-\pi\kappa_h f}$. The site term for the horizontal component in this case is $S(f)$ = H/V. The common case is when the κ_v is not zero and not identical to κ_h. In this general case a portion of κ value ($\Delta\kappa = \kappa_h - \kappa_v$) has already been included in the H/V ratio; thus, it should be subtracted from the near-surface attenuation term for the horizontal component. Hence, the site term for the horizontal component can be considered (G. Atkinson, personal comm., 2006) as

$$S(f) = \text{H/V}e^{-\pi(\kappa_h - \Delta\kappa)f} = \text{H/V}e^{-\pi\kappa_v f}. \quad (5)$$

Figure 7 shows the site effect, $S(f) = \text{H/V}e^{-\pi\kappa_v f}$, for BHRC stations in northern Iran compared with those of generic rock (V_{s30} = 620 m/sec) and soil (V_{s30} = 310 m/sec) site classes (Boore and Joyner, 1997). The amplifications for generic soil and rock sites (Boore and Joyner, 1997) were multiplied by $\exp(-\pi f\kappa)$, where κ = 0.035 for California sites. Despite the ambiguity in this approach, the trend of residuals at frequencies greater than 5 Hz, which is discussed in the following sections and shown in Figures 8c and d, confirms this decision.

All the previously mentioned regional key seismic parameters estimated in this study are used in the simulation of the acceleration time series based on the stochastic modeling approach to estimate the stress drop for earthquakes in northern Iran, as discussed in the following sections.

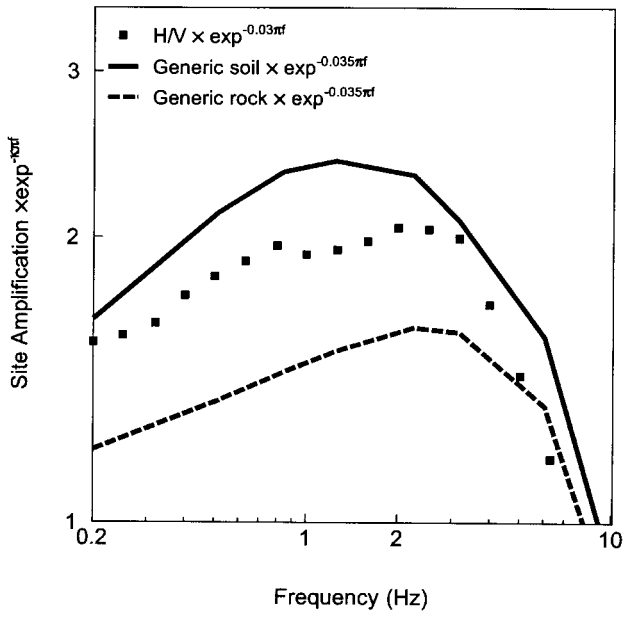

Figure 7. Site effects, $S(f) = \text{H/V}e^{-\pi\kappa_v f}$, for the horizontal components of the BHRC stations in northern Iran in comparison with those of generic rock (V_{s30} = 620 m/sec) and soil (V_{s30} = 310 m/sec) site classes (Boore and Joyner, 1997). The amplifications for generic soil and rock sites were multiplied by $\exp(-\pi f\kappa)$, where κ = 0.035 for sites in California.

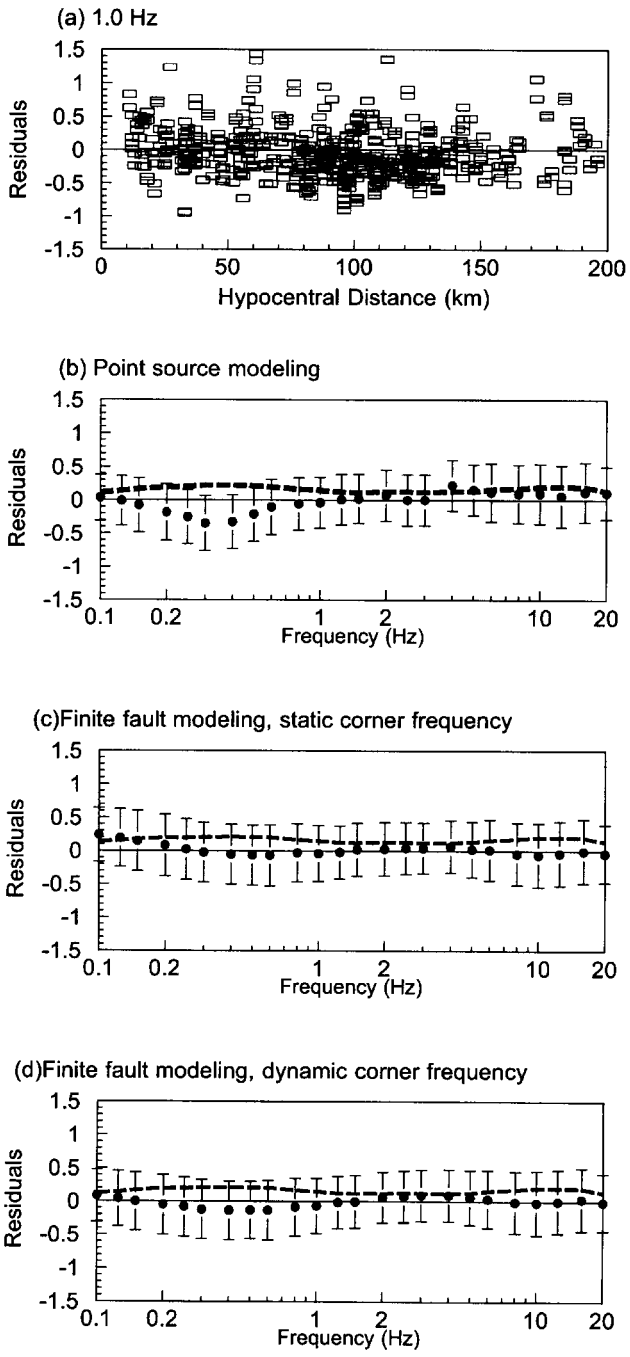

Figure 8. (a) The distribution of residuals for 1.0 Hz versus distance for the best-case scenario of point-source modeling. (b) Minimized MSE and the mean value of residuals over all frequencies for the best-case scenario of point-source modeling. (c) Minimized MSE and the mean value using finite-fault modeling based on static corner frequency. (d) Same as c with dynamic corner frequency model. Error bars show ±1 S.D.

Estimation of Stress Drop

In this study, three stochastic modeling approaches are applied to estimate stress drop for earthquakes in northern Iran: (1) point source (e.g., Boore, 1983); (2) finite-fault approaches using a static corner frequency (Beresnev and Atkinson, 1998a; Motazedian and Atkinson, 2005b); and (3) finite fault using a dynamic corner frequency (Motazedian and Atkinson, 2005b).

Point-Source Modeling

In stochastic point-source modeling, the acceleration spectrum follows an ω^2 shape for a fault at a distance R which is modeled as a point source (Aki, 1967; Brune, 1970, 1971; Boore 1983). The acceleration spectrum of the shear wave, $A(f)$, is described by

$$A(f) = CM_0 \frac{(2\pi f)^2}{\left[1 + \left(\frac{f}{f_0}\right)^2\right]} e^{\frac{-\pi f R}{Q(f)\beta}} R^b D(f) e^{-\pi f \kappa_0}, \quad (6)$$

where the constant $C = \Re^{\theta\varphi} FV/(4\pi\rho\beta^3)$. $\Re^{\theta\varphi}$, F, V, ρ, β, M_0, and b are the radiation pattern (average value of 0.55 for shear waves), the free-surface amplification (2.0), the partition onto two horizontal components (0.71), density, shear-wave velocity, seismic moment, and geometric spreading factor, respectively. $b = -1$ is applicable for body-wave spreading in a whole space. The corner frequency, f_0, is calculated from

$$f_0 = 4.9 \times 10^6 \beta \left(\frac{\Delta\sigma}{M_0}\right)^{1/3}, \quad (7)$$

where $\Delta\sigma$ is stress drop in bars, and β is shear-wave velocity in kilometers per second. The quality factor, Q (f), is inversely related to anelastic attenuation. $D(f)$ is the site amplification and $\exp(-\pi f\kappa_0)$ is a high-cut filter used to include the effect of κ_0.

The approach of the stochastic point-source model is to generate a transient time series that has a stochastic character, with an average of the spectra for many realizations matching a specified desired amplitude spectrum (Boore, 1983). A window is applied to a time series of Gaussian noise with zero mean and unit variance. The windowed time series is transformed to the frequency domain and the amplitude spectrum of the random time series is multiplied by the desired spectrum. Transformation back to the time domain results in a stochastic time series whose amplitude spectrum is the same as the desired spectrum on average (Boore, 1983, 1996, 2003).

The previously mentioned regional key seismic parameters are used in the simulation of the acceleration time series. Some general values are considered in this simulation. Crustal shear-wave velocity and crustal density are considered to be 3.6 km/sec and 2.8 (g/cm^3), respectively. The duration of ground motion is generally represented as $T(R) = T_0 + dR$, where T_0 is the source duration (T_0 = fault length/rupture velocity), and d is the coefficient controlling the increase of duration with distance. A generic value of 0.1 is good for d to control the increase of duration with distance (Beresnev and Atkinson, 2002).

By using the region-specific key seismic parameters and the general parameters described previously, a synthetic acceleration time series can be simulated corresponding to each individual accelerographic record from the BHRC. The stochastic point-source modeling is iterated over a wide range of values for stress drop, the only unknown parameter in equations (6) and (7). The frequency content of each simulated acceleration time series is compared with the actual record by the calculation of residuals. Residuals are defined as the log of observed PSA minus the log of predicted PSA (where PSA is the horizontal component 5% damped pseudo-acceleration). Residuals for frequencies from 0.1 Hz to 20 Hz over all records are calculated. The distribution of residuals was plotted versus distance (as an example, Fig. 8a for 1 Hz) to rule out a trend versus distance. The applied geometric spreading factors in the time series simulation provide reasonable results with the observed records. The mean-square error, MSE $= \frac{1}{n}\sum (\mathrm{PSA}_{\mathrm{observed}} - \mathrm{PSA}_{\mathrm{simulated}})^2$ and the mean value of residuals for each frequency are calculated. The goal is to find the stress drop that provides the minimum MSE, whereas increasing the stress drop will shift almost the entire distribution of residuals in Figure 8b downward and decreasing the stress drop shifts the distribution upward. Stress drop of 125 bars provides the minimum MSE and the mean values fluctuating around the zero line with a maximum standard deviation of 0.46 as shown in Figure 8b, which provides the mean value and MSE of residuals versus frequency (error bars in Fig. 8b show $\pm$ 1 S.D.).

Point-source modeling of earthquake ground motion may not be appropriate for large earthquakes, because the effects of a large fault plane, including fault geometry, heterogeneity of slip on the fault plane, and directivity, can influence the amplitudes, frequency content, and duration of ground motion. A two-corner model has also been proposed by Atkinson (1993) to represent finite-fault effects that are important for large events. In the two-corner model, the source term is given by

$$A(f) = CM_0(2\pi f)^2 \left\{ \frac{(1-\varepsilon)}{\left[1 + \left(\frac{f}{f_a}\right)^2\right]} + \frac{\varepsilon}{\left[1 + \left(\frac{f}{f_b}\right)^2\right]} \right\}, \quad (8)$$

where the parameters ε, f_A, and f_B are region-specific parameters (Atkinson and Boore, 1995) and for eastern North America are given by

$$\log(\varepsilon) = 2.52–0.637\mathbf{M} \quad (9)$$

$$\log(f_A) = 2.41–0.533\mathbf{M} \quad (10)$$

$$\log(f_B) = 1.43–0.188\mathbf{M}. \quad (11)$$

For large earthquakes the stochastic method with a two-corner source has been shown to best represent the source spectrum (Atkinson and Boore, 1995), but despite the superior advantages of the two-corner frequency over the Brune model, in this section we are interested in the estimation of stress drop, which can not be calculated from the two-corner model. We further check the stress-drop values by using finite-fault modeling, which has been another tool for the prediction of ground motion near the epicenters of large earthquakes (Hartzel, 1978; Irikura, 1983; Joyner and Boore, 1986; Beresnev and Atkinson, 1998a,b; Motazedian and Atkinson, 2005a,b; Motazedian and Moinfar, 2006). The next section describes the applied stochastic finite-fault modeling based on a static corner frequency.

Finite-Fault Modeling Based on Static Corner Frequency

In finite-fault modeling, a large fault is divided into N subfaults ($N = nl * nw$, where nl and nw are the number of subfaults along the length and width of main fault, respectively) and each subfault is considered to be a small point source (introduced by Hartzell, 1978). The rupture spreads radially from the hypocenter. In our implementation the ground motions of subfaults, each of which is calculated by the stochastic point-source method described in the previous section, are summed to obtain the ground-motion acceleration. The acceleration spectrum for a subfault can be modeled as a point source with an ω^2 shape (Aki, 1967; Brune, 1970, 1971; Boore 1983). In this approach equation (6) is used to obtain the acceleration spectrum of the shear wave for each subfault. In the application of equation (6) for the ijth subfault $A(f)$, f_0, R, and M_0 are replaced by $A_{ij}(f)$, f_{0ij}, R_{ij}, and M_{0ij}, where they are the acceleration spectrum of shear wave, corner frequency, distance from the observation point and the seismic moment of the ijth subfault, respectively. The corner frequency of the ijth subfault, $f_{0ij}(t)$, is defined as

$$f_{0ij} = 4.9 \times 10^6 \beta \left(\frac{\Delta\sigma}{M_{0\text{ave}}}\right)^{1/3} = 4.9 \times 10^6 N^{1/3} \beta \left(\frac{\Delta\sigma}{M_0}\right)^{1/3}, \quad (12)$$

where the average seismic moment of subfaults in dyne cm is $M_{0\text{ave}} = M_0/N$. In identical subfaults, the moment of each subfault is controlled by the ratio of its area to the area of the main fault ($M_{0ij} = M_0/N$, where M_0 is the seismic moment of the entire fault). If the subfaults are not identical the seismic moment of each subfault is expressed as

$$M_{0ij} = \frac{M_0 S_{ij}}{\sum_{l=1}^{nl} \sum_{k=1}^{nw} S_{ki}}, \quad (13)$$

where S_{ij} is the relative slip weight of the ijth subfault (Beresnev and Atkinson, 1998a,b; Motazedian and Atkinson, 2005b). The ground motions of the subfaults are summed in the time domain to obtain the ground-motion acceleration of the entire fault, $a(t)$

$$a(t) = \sum_{i=1}^{nl} \sum_{j=1}^{nw} A_{ij}(t + \Delta t_{ij}), \quad (14)$$

where Δt_{ij} is the relative delay time for the radiated wave from the ijth subfault to reach the observation point. This approach has been implemented in the EXSIM (EXtended fault SIMulation) program (Motazedian and Atkinson, 2005b). Application of stochastic finite-fault modeling based on static corner frequency in EXSIM slightly differs from its precedent, FINSIM (stochastic FINite fault SIMulation; Beresnev and Atkinson, 1998a), in the calculation of corner frequency and seismic moment of each subfault.

EXSIM was used to simulate synthetic waveforms for each actual record of the BHRC. The dimensions of each fault are calculated based on Wells and Coppersmith (1994). Input parameters to EXSIM are given in Table 2. Note that the b-values needed for the finite-fault simulation should be suitable for subfaults that are comparable to earthquakes with magnitude **M** 4, or **M** 5. The b-value for the first segment of trilinear behavior (distances up to 70 km in this study) was obtained under the influence of near-source and finite-fault effects, because most of the database originates from earthquakes with magnitudes greater than **M** 6.0. Hence, $b = -0.6$ is not suitable for the first segment of the trilinear behavior. Thus, a theoretical geometric spreading factor, $b = -1$, for point source is considered for the first segment of trilinear behavior of geometric spreading. This selection is confirmed by the symmetrical distribution of residuals around a zero line for near-source distances. To cover all of the possible backward, forward, and null directivity regions for each BHRC record a profile with a fixed closest distance to the fault is considered. Each profile covers 15 values of azimuth from 0 to 180 degrees. In addition, a total of five random hypocenters are considered for each earthquake ($15 * 5 = 75$, a total of 75 simulated records for each actual BHRC record).

The same procedure that was applied in stochastic point-source modeling is applied to calculate residuals in this approach as well. The distribution of residuals averaged over all events versus frequency is shown in Figure 8c. The best value for the stress drop to produce the minimum MSE is 68 bars. Error bars in Figure 8c are $\pm$ 1 S.D. The mean value line is very close to zero at frequencies above 1 Hz with the maximum standard deviation of 0.48 but deviates from the zero line at lower frequencies.

Table 2
Stochastic Model Input Parameters for EXSIM

Parameter	Point Source	Static Corner Frequency	Dynamic Corner Frequency
Stress drop	125 bars	68 bars	68 bars
$Q(f)$	$\log(Q) = 1.99 (\log f)^2 - 0.67 (\log f) + 2.32$	$\log(Q) = 1.99 (\log f)^2 - 0.67 (\log f) + 2.32$	$\log(Q) = 1.99 (\log f)^2 - 0.67 (\log f) + 2.32$
Duration	$T_0 + 0.1$ (km)	$T_0 + 0.1$ (km)	$T_0 + 0.1$ (km)
Site effects	$\mathrm{H/V}e^{-\pi\kappa_v f}$	$\mathrm{H/V}e^{-\pi\kappa_v f}$	$\mathrm{H/V}e^{-\pi\kappa_v f}$
K_v	0.03	0.03	0.03
Fault width	NA	based on Wells and Coppersmith (1994)	based on Wells and Coppersmith (1994)
Pulsing area percentage	NA	NA	50%
Windowing function	Saragoni-Hart	Saragoni-Hart	Saragoni-Hart
Geometric spreading*	$R^{-1.0}$ ($R < 70$ km) $\mathrm{R}^{+.2}$ (70 km $\le R \le$ 150) $\mathrm{R}^{-.1}$ (150 km $< R$)	$R^{-1.0}$ ($R < 70$ km) $R^{+.2}$ (70 km $\le R \le$ 150) $R^{-.1}$ (150 km $<$ R)	$R^{-1.0}$ ($R < 70$ km) $R^{+.2}$ (70 km $\le R \le$ 150) $R^{-.1}$ (150 km $< R$)
Rupture velocity	NA	0.8 of β	0.8 of β
Slip distribution	NA	random	random

A theoretical geometric spreading factor, $b = -1$, for point source is considered for the first segment of trilinear behavior of geometric spreading. This selection is confirmed by the symmetrical distribution of residuals around zero line for near-source distances.

Stochastic finite-fault modeling based on dynamic corner frequency is able to improve the behavior of residuals at lower frequencies (Motazedian and Atkinson, 2005b; Motazedian and Moinfar, 2006), which is applied in the next section.

Finite-Fault Modeling Based on Dynamic Corner Frequency

The approach of stochastic finite-fault modeling based on dynamic corner frequency is similar to the static corner frequency modeling described in the previous section, but the corner frequencies of the subfaults are a function of time. In this approach the acceleration spectrum of the shear wave of the ijth subfault, $A_{ij}(f)$, is described by

$$A_{ij}(f) = CM_{0ij} H_{ij} \frac{(2\pi f)^2}{\left[1 + \left(\frac{f}{f_{0ij}(t)}\right)^2\right]} e^{\frac{-\pi f R_{ij}}{Q(f)\beta}} R_{ij}^{b} D(f) e^{-\pi f \kappa_0} \quad (15)$$

where the dynamic corner frequency, $f_{0ij}(t)$, is defined as a function of the cumulative number of ruptured subfaults, $N_R(t)$, at time t:

$$f_{0ij}(t) = 4.9 \times 10^6 N_R^{-1/3} N^{1/3} \beta \left(\frac{\Delta\sigma}{M}\right)^{1/3}. \quad (16)$$

H_{ij} is a scaling factor that is applied to conserve the total area under the spectrum of subfaults as the corner frequency decreases with time (Motazedian and Atkinson, 2005b). Note that the dependence of $f_{0ij}(t)$ on time and H_{ij} are the only differences between equations (16) and (6). The scaling factor, H_{ij}, is given by

$$H_{ij} = \left(N\Sigma\left\{f^2/[1 + (f/f_0)^2]\right\}^2/\Sigma \left\{f^2/[1 + (f/f_{0ij})^2]\right\}^2\right)^{1/2}. \quad (17)$$

Because the scaling factor, H_{ij}, changes the spectrum at all frequencies, the amplitude of the spectrum at low frequencies, which represents the seismic moment, is changed. In EXSIM, H_{ij} is tapered such that it gradually approaches unity at low frequencies; thus, the seismic moment is conserved. The practical effect of this taper function on the time series and response spectra in the frequency range of engineering interest is negligible. Motazedian and Atkinson (2005b) have shown that the influence of the scaling factor on lower frequencies is typically small.

In actual earthquake ruptures, the slip may only be occurring on some part of the fault, whereas the other areas on the fault are passive. In EXSIM only the active area contributes to the dynamic corner frequency at a given moment in time, and therefore the passive area does not affect the dynamic corner frequency. In our implementation of this concept, the cumulative number of pulsing subfaults, as given

by N_R in equation (16), would increase with time at the beginning of rupture but become constant at some fixed percentage of the total rupture area. This percentage is referred to as the "%pulsing area." This parameter can be used to adjust the level of spectrum at lower frequencies (Motazedian and Atkinson, 2005b).

Similar to the approach taken in the last section for the application of static corner, 75 synthetic records were simulated for each BHRC record to estimate stress drop based on the region-specific key seismic parameters. All other EXSIM parameters in the application of dynamic corner frequency have been described previously and given in Table 2. In the first step, we change the stress drop to adjust the amplitude of higher frequencies and in the second step we adjust the amplitude of lower frequencies by varying the percentage of pulsing area. The lowest residuals averaged over all events and all frequencies are shown in Figure 8d. The minimum MSE is provided by the stress drop of 68 bars. The average residual is close to zero at all frequencies with the maximum standard deviation of 0.47. The close-to-zero distribution of residuals in Figure 8d displays good agreement between simulated and observed data, which gives us enough confidence in the overall trend of our simulated acceleration time series.

To evaluate the assumed generic geometric spreading factor for the study area, the distribution of residuals versus distance is plotted for 1 Hz and shown in Figure 9a. The distribution of residuals versus magnitude in Figure 9b shows a trend beyond **M** 6.5, where data are very sparse and can not be judged.

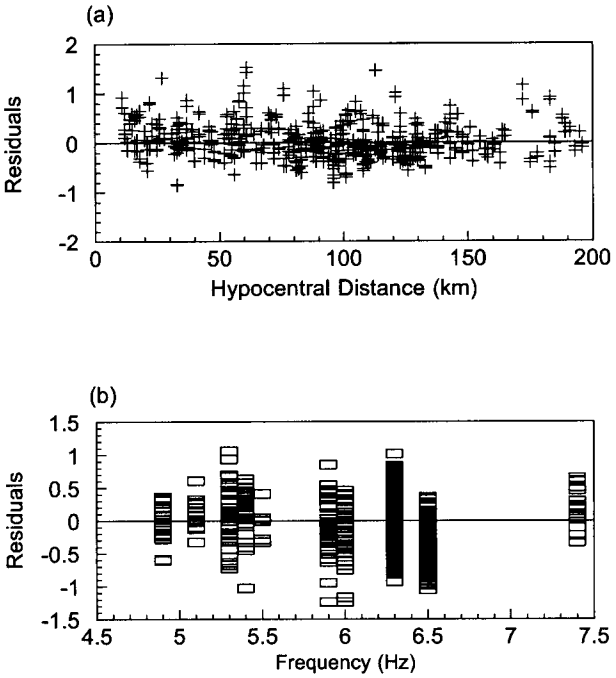

Figure 9. (a) Distribution of residuals versus distance for 1.0 Hz. (b) The distribution of residuals versus magnitude for 1.0 Hz. Note that beyond **M** 6.5 the data are sparse and cannot be judged.

Conclusions

Acceleration time series of 22 earthquakes recorded on BHRC strong-motion stations were processed and analyzed to obtain region-specific key seismic parameters. Fourier amplitude spectra were used to determine geometric spreading model and anelastic attenuation by using a maximum likelihood regression method. These parameters are mainly derived from the vertical component, assuming that the vertical component is less affected by the site condition than the horizontal components, because there is no site-specific information on BHRC stations. A trilinear geometric spreading model is suggested by the analysis of residuals with hinges at 70 km and 150 km. The regional Q-value is $Q = 87 f^{1.46}$ based on the obtained trilinear geometric spreading model for the region.

The distance-dependent kappa factors, for both horizontal and vertical components, were obtained from the slope of the smoothed amplitude of Fourier acceleration spectrum at higher frequencies. The κ_0 for horizontal and vertical components are 0.05 and 0.03, respectively. The clear difference between vertical and horizontal κ_0 values suggests that there should be a distinguishable near-surface site-attenuation effect on the horizontal components compared with the vertical component.

The ratio of the H/V component of ground motion is considered to be a rough estimate of site amplification. The overall site term, which is the site amplification multiplied by the near-surface attenuation, can be considered to be $\mathrm{H/V}e^{-\pi\kappa_v f}$, because a portion of the kappa value has already been included in the H/V ratio. Despite ambiguity in the theory of this approach, the trend of residuals at frequencies greater than 5 Hz confirms this decision. The overall site effect for BHRC staions in northern Iran follows the general trend of generic soil-site effect (Boore and Joyner, 1997) with lower amplitudes.

After the calculation of the earlier mentioned regional key seismic parameters, three stochastic approaches were applied to estimate stress drop for the study region. Stochastic point-source modeling, suggests stress drop of 125 bars, whereas stochastic finite-fault modeling, using both static and dynamic corner frequencies, suggests 68 bars. Finite-fault modeling based on static corner frequency provides a better close-to-zero distribution of residuals over higher frequencies than point-source modeling, because the effects of a large finite source are considered in this approach.

The most frequent criticism of finite-fault modeling based on the static corner frequency approach, including those by Schneider *et al.* (1993), Silva and Darragh (1995), and Beresnev and Atkinson (1998a, 1999, 2000, 2002), has been that the results depend on the selected subfault sizes. In addition, simulated near-source acceleration time series for large earthquakes often contain artificial gaps due to the

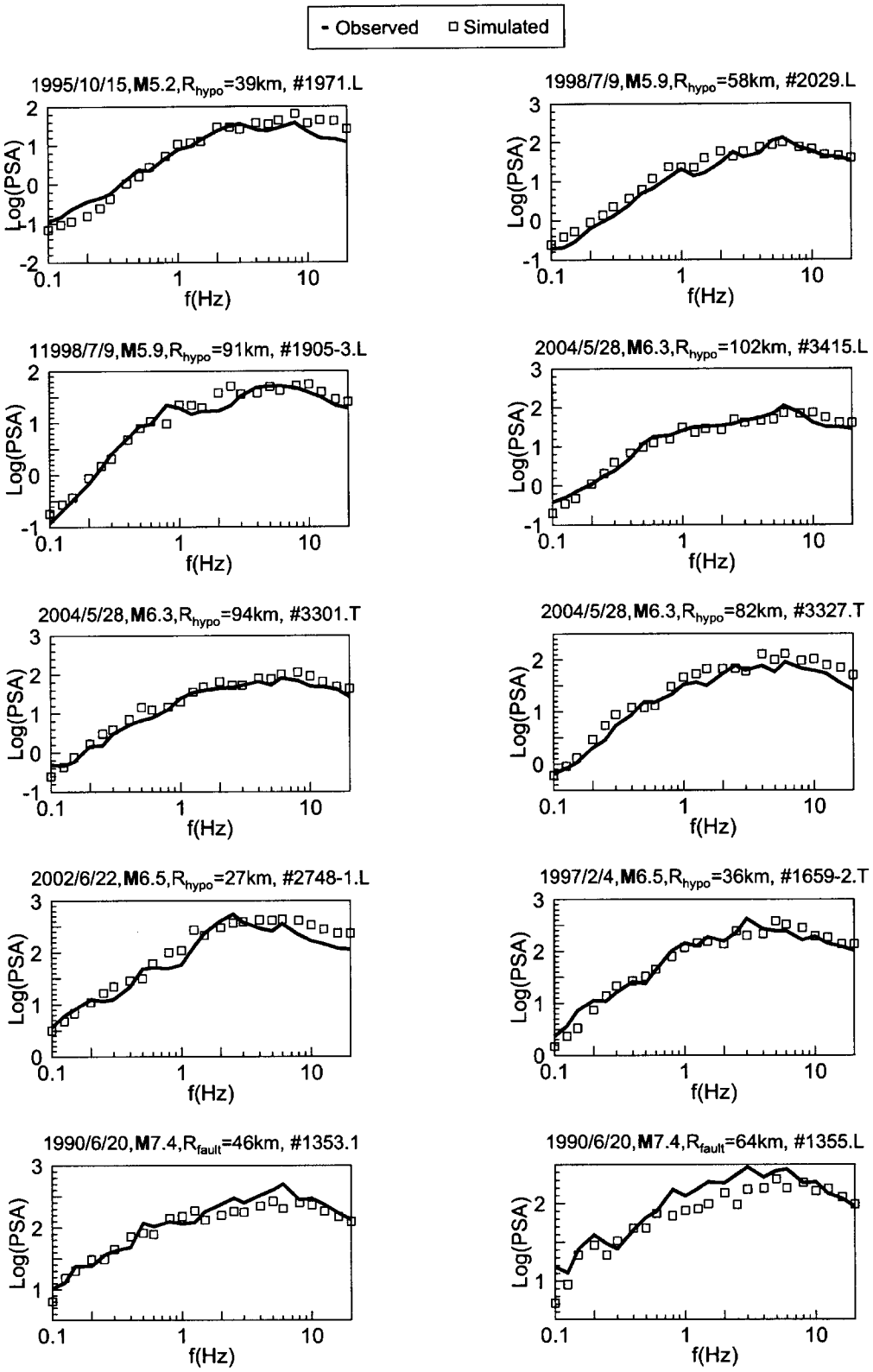

Figure 10. Some of simulated times series for magnitudes from **M** 5.2 to **M** 7.4 where the response spectrum closely follows the spectrum of the recorded spectrum.

large subfault size. The stochastic finite-fault modeling based on dynamic corner frequency offers several advantages over previous stochastic finite-fault models, which has been described by Motazedian and Atkinson (2005b). To avoid production of gaps in the near-source acceleration time series due to the subfault-size dependence of the static corner frequency approach, stochastic finite-fault modeling based on a dynamic corner frequency was applied. The behavior of residuals confirms that a better agreement between the observed and simulated spectra at lower frequencies is produced with the application of dynamic corner frequency.

The distribution of residuals shows that the simulated time series in some cases is far from the recorded time series. This is because of two main facts: (1) All of BHRC sites, including any possible rock site along with all other soil types, were treated equally in terms of site effects because of the lack of site-specific information. Site effects by themselves place a considerable wide range of residuals even in well-studied seismic stations. (2) The fault geometry of the main part of database is unknown, but the distribution of residuals suggests that the simulated time series on average are reasonable compared with the recorded series. Figure 10 shows some example spectra where the simulated and observed series are similar for a wide of magnitude from **M** 5.2 to **M** 7.4.

Acknowledgments

I thank the Building and Housing Research Centre of Iran for providing the accelerographic database. I also thank Gail Atkinson and Eleanor Sonley for helpful discussion. I am grateful to David M. Boore and other anonymous reviewers for their reviews and comments, which significantly improved this article. I thank Majid Behnam, Fereidoon Sinaiean, Hadi Khademi, and Ebrahim Maleki for providing useful information.

References

Aki, K. (1967). Scaling law of seismic spectrum, *J. Geophys. Res.* **72,** 1217–1231.

Aki, K. (1980). Attenuation of shear waves in the lithosphere for frequencies from 0.05 to 25 Hz, *Phys. Earth Planet. Interiors* **21,** 50–60.

Anderson, J., and S. Hough (1984). A model for the shape of the Fourier amplitude spectrum of acceleration at high frequencies, *Bull. Seism. Soc. Am.* **74,** 1969–1993.

Anderson, J. G., Y. Zeng, and H. Sucuoglu (2001). Analysis of accelerations from the 1 October 1995 Dinar, Turkey, earthquake, *Bull. Seism. Soc. Am.* **91,** 1433–1445.

Atkinson, G. M. (1993). Source spectra for earthquakes in eastern North America, *Bull. Seism. Soc. Am.* **83,** 1778–1798.

Atkinson, G. M. (2004). Empirical attenuation of ground-motion spectral amplitudes in southeastern Canada and the northeastern United States, *Bull. Seism. Soc. Am.* **94,** 1079–1095.

Atkinson, G. M., and D. M. Boore (1995). New ground motion relations for eastern North America, *Bull. Seism. Soc. Am.* **85,** 17–30.

Atkinson, G. M., and J. Cassidy (2000). Integrated use of seismograph and strong motion data to determine soil amplification in the Fraser Delta: results from the Duvall and Georgia Strait earthquakes, *Bull. Seism. Soc. Am.* **90,** 1028–1040.

Atkinson, G. M., and R. Mereu (1992). The shape of ground motion attenuation curves in southeastern Canada, *Bull. Seism. Soc. Am.* **82,** 2014–2031.

Atkinson, G. M., and W. Silva (1997). Empirical source spectra for California earthquakes, *Bull. Seism. Soc. Am.* **87,** 97–113.

Berberian, M. (1976). Contribution to the seismotectonics of Iran (part 2), Geological Survey of Iran, Report 39.

Beresnev, I., and G. M. Atkinson (1997). Shear wave velocity survey of seismographic sites in eastern Canada: calibration of empirical regression method of estimating site response, *Seism. Res. Lett.* **68,** 981–987.

Beresnev, I., and G. M. Atkinson (1998a). FINSIM—a FORTRAN program for simulating stochastic acceleration time histories from finite faults, *Seism. Res. Lett.* **69,** 27–32.

Beresnev, I., and G. M. Atkinson (1998b). Stochastic finite-fault modeling of ground motions from the 1994 Northridge, California earthquake, part I: validation on rock sites, *Bull. Seism. Soc. Am.*, **88,** 1392–1401.

Beresnev, I., and G. M. Atkinson (1999). Generic finite-fault model for ground motion prediction in eastern North America, *Bull. Seism. Soc. Am.* **89,** 608–625.

Beresnev, I., and G. M. Atkinson (2000). Subevent structure of large earthquakes—a ground motion perspective, *Geophys. Res. Lett.* **28,** 53–56.

Beresnev, I., and G. M. Atkinson (2002). Source parameters of earthquakes in eastern and western North America based on finite-fault modeling, *Bull. Seism. Soc. Am.* **92,** 695–710.

Boore, D. M. (1983). Stochastic simulation of high-frequency ground motions based on seismological models of the radiated spectra, *Bull. Seism. Soc. Am.* **73,** 1865–1894.

Boore, D. M. (1996). SMSIM—Fortran programs for simulating ground motions from earthquakes, *U.S. Geol. Surv. Open-file Report 96-80-A*.

Boore, D. M. (2003). Simulation of ground motion using the stochastic method, *Pure Appl. Geophys.* **160,** 636–676.

Boore, D. M., and W. B. Joyner (1997). Site amplifications for generic rock sites. *Bull. Seism, Soc. Am.* **87,** 327–341.

Boore, D. M., W. B. Joyner, and L. Wennerberg (1992). Fitting the stochastic omega-squared source model to observed response spectra in western North America: trade-offs Between $\Delta\sigma$ and κ, *Bull. Seism. Soc. Am.* **82,** 1956–1963.

Brune, J. (1970). Tectonic stress and the spectra of seismic shear waves from earthquakes, *J. Geophys. Res.* **75,** 4997–5009.

Brune, J. (1971). Correction to Brune (1970), *J. Geophys. Res.* **76,** 5002.

Building and Housing Research Center (BHRC) (2005) http://www.bhrc.ac.ir/ (last accessed December 2005).

Burger, R., P. Somerville, J. Barker, R. Herrmann, and D. Helmberger (1987). The effect of crustal structure on strong ground motion attenuation relations in eastern North America, *Bull. Seism. Soc. Am.* **77,** 420–439.

Cormier, V. (1982). The effect of attenuation on seismic body waves, *Bull. Seism. Soc. Am.* **72,** S169–S200.

Hartzell, S. (1978). Earthquake aftershocks as Green's functions, *Geophys. Res. Lett.* **5,** 1–14.

Harvard Seismology (2006). Centroid Moment Tensor (CMT) catalog search, www.seismology.harvard.edu/(last accessed December 2005).

Herrmann, R., and A. Kijko (1983). Modeling some empirical vertical component *Lg* relations, *Bull. Seism. Soc. Am.* **73,** 157–171.

Irikura, K. (1983). Semi-empirical estimation of strong ground motions during large earthquakes, *Bull. Disaster Prevention Res. Inst.*, Kyoto Univ. **33,** 63–104.

Joyner, W., and D. M. Boore (1986). On simulating large earthquakes by Green's function addition of smaller earthquakes, in *Earthquake Source Mechanics*, M. Ewing (Editor), American Geophysical Monograph **37,** 269–274.

Joyner, W. B., and D. M. Boore (1993). Methods for regression analysis of strong motion data, *Bull. Seism. Soc. Am.* **83,** 469–487.

Joyner, W. B., and D. M. Boore (1994). Errata on Joyner and Boore (1993), *Bull. Seism. Soc. Am.* **84,** 955–956.

Khademi, M. R., and A. Nayeri (1997). Seismotectonic provinces of Iran, Iranian Committee on Large Dams Bulletin 6.

Lermo, J., and F. Chavez-Garcia (1993). Site effect evaluation using spectral ratios with only one station, *Bull. Seism. Soc. Am.* **83,** 1574–1594.

Mirzaei, N., M. T. Gao, and Y. T. Chen (1999). Delineation of potential seismic sources for seismic zoning of Iran, *J. Seism.* **3,** no. 1, 17–30.

Motazedian, D., and G. M. Atkinson (2005a). Ground motion relations for Puerto Rico, Geological Society of America bulletin, GSA, **385,** 61–80.

Motazedian, D., and G. M. Atkinson (2005b). Stochastic finite-fault modeling based on a dynamic corner frequency, *Bull. Seism. Soc. Am.* **95,** 995–1010.

Motazedian, D., and A. A. Moinfar (2006). Hybrid stochastic finite fault modeling of 2003, M6.5, Bam Earthquake (Iran), *J. Seism.* (in press).

Nakamura, Y. (1989). A method for dynamic characteristics estimation of subsurface using microtremor on the ground surface, *QR RTRI* **30,** 25–33.

Nowroozi, A. (1976). Seismotectonic provinces of Iran, *Bull. Seism. Soc. Am.* **66,** 1249–1276.

Raoof, M., R. Herrmann, and L. Malagnini (1999). Attenuation and excitation of three-component ground motion in southern California, *Bull. Seism. Soc. Am.* **89,** 888–902.

Schneider, J., W. Silva, and C. Stark (1993). Ground motion model for the 1989 M 6.9 Loma Prieta earthquake including effects of source, path and site, *Earthquake Spectra* **9,** 251–287.

Siddiqqi, J., and G. M. Atkinson (2002). Ground motion amplification at rock sites across Canada, as determined from the horizontal-to-vertical component ratio, *Bull. Seism. Soc. Am.* **92,** 877–884.

Silva, W., and R. Darragh (1995). Engineering characterization of strong ground motion recorded at rock sites, Electric Power Res. Inst. Report TR-102262.

Sokolov, V. Y., C. H. Loh, and K. L. Wen (2002). Comparison of the Taiwan Chi-Chi earthquake strong-motion data and ground-motion assessment based on spectral model from smaller earthquakes in Taiwan, *Bull. Seism. Soc. Am.* **92,** 1855–1877.

Stocklin, J. (1968). Structural history and tectonics of Iran: a review, *Bull. Am. Assoc Petrol. Geol.* **52,** 1229–1258.

Takin, M. (1972). Iranian geology and continental drift in the Middle East, *Nature* **235,** no. 5334, 147–150.

Wells, D., and K. Coppersmith (1994). New empirical relationships among magnitude, rupture length, rupture width, rupture area, and surface displacement, *Bull. Seism. Soc. Am.* **84,** 974–1002.

Department of Earth Science
Carleton University
Ottawa, Ontario, K1S5B6, Canada
dariush@ccs.carleton.ca

Manuscript received 28 July 2005.